Twist Response of Actin Filaments

Jeffrey P. Bibeau, Nandan G. Pandit, Shawn Gray, Nooshin Shatery Nejad, Charles V. Sindelar, Wenxiang Cao, Enrique M. De La Cruz[*]

Department of Molecular Biophysics and Biochemistry, Yale University, New Haven, CT, 06520

*To whom correspondence should be addressed.

Supplementary Information:

Materials and Methods

Samples were prepared and experiments carried out in KMI buffer (10 mM fluorescence-grade imidazole pH 7.0, 50 mM KCl, 2 mM $MgCl_2$, 0.2 mM ATP, 2 mM DTT) supplemented with 15 mM glucose, 0.02 mg mL^{-1} catalase, and 0.1 mg mL^{-1} glucose oxidase.

Coverslip Functionalization and Microfluidics
Surface functionalization and passivation of microscope coverslips with 2-5% Biotin labeled PEG-Silane slides were adapted from elsewhere (1). Coverslips were cleaned by sonication in a 2% Hellmanex solution for 30 min using a sonicating water bath, rinsed exhaustively with Milli-Q water, sonicated for 30 min in 2 M HCl, rinsed exhaustively with MilliQ water, then sonicated in 1 M NaOH for 45 min to hydroxylate the surface. To ensure the coverslip surface was anhydrous, coverslips were dried with compressed nitrogen and placed in a convection oven for 10 min at 90 °C. Coverslips were subsequently sonicated in acetone for 5 min, air-dried and placed onto PDMS molds. Coverslips and PDMS molds were heated at 90 °C for 10 min. 800 μL of a 25% PEG silane and 2-5% biotin PEG mixture in DMSO was pipetted onto the coverslips and incubated at 90 °C for 15 min in a glass Petri dish. Coverslips were removed from the molds, rinsed with MilliQ water, dried with compressed nitrogen, vacuum sealed in 50 mL Falcon tubes, stored at 4 °C, and used within 2 weeks.

Microfluidic chambers were assembled as described (2, 3). Briefly, parafilm was sandwiched between microfluidic chambers and functionalized coverslips and subsequently bonded with heat. Microfluidic channels were incubated with Tween 20 for 10 min, washed with 200 μL T50 buffer (50 mM NaCl and 10 mM Tris pH 8), incubated with 200 μL of 100 μg mL^{-1} of neutravidin in T50 buffer for 10 min, and washed with 200 μL 1X KMI buffer.

Coating Paramagnetic Beads with Anti-Digoxigenin Antibody
Superparamagnetic Dynabeads™ M-270 Epoxy (2.8 μm in diameter, Thermo-Fisher catalog #14301) were conjugated to anti-digoxigenin antibody following the company-provided protocol. Briefly, a 10 mg mL^{-1} suspension of beads was washed 5 times with 1 mL Buffer A (0.1 M sodium phosphate, pH 7.4). Beads were pelleted during wash steps by placing a permanent magnet at the bottom of the Eppendorf tube and remained immersed to avoid air exposure. A 100 μL suspension of beads in Buffer A was mixed with 100 μL of a 400 μg mL^{-1} anti-digoxigenin antibody solution (Thermo/Invitrogen catalog # PA1-85378). 100 μL of 3 M ammonium sulfate was subsequently added to yield a final volume of 300 μL. This bead suspension solution was rotated at 37 °C for 2 h before washing 5 times with 1 mL of Buffer A supplemented with 0.5 mg mL^{-1} fatty acid-free BSA (Sigma catalog # A7030) that had been filtered with a

0.2 µm low protein-binding filter (Millipore Millex-GV PVDF). Coated beads were suspended in 300 µL of Buffer A supplemented with 0.5 mg mL^{-1} filtered fatty-acid free BSA and stored at 4 °C.

Filament Bead Conjugation
Ca^{2+}-actin monomers (unlabeled, Alexa 488-, Alexa 647-, biotin-, or digoxigenin-labeled) were converted to Mg^{2+}-actin monomers with 0.2mM EGTA and 50 µM MgCl$_2$ on ice before polymerization (4). Mg^{2+}-actin monomers (10% biotinylated, 15% Alexa 488- or Alexa 647-labeled, and 75% unlabeled) were polymerized with addition of 0.1 volume of 10X polymerizing buffer (100 mM fluorescence-grade imidazole pH 7.0, 500 mM KCl, 20 mM MgCl$_2$), and ATP and DTT at a final concentration of 0.2 and 2 mM, respectively.

These fluorescent, biotinylated filaments were diluted to 100-200 nM in KMI buffer supplemented with 15 mM glucose, 0.02 mg mL^{-1} catalase, and 0.1 mg mL^{-1} glucose oxidase, sheared by gently pipetting up and down 10 times with a P200 pipette, mixed with 1.5 µM (final concentration after mixing) of 15% Alexa 488- or Alexa 647-labeled Mg^{2+}-actin monomers, and equilibrated for 2-2.5 minutes to allow filaments to elongate. This procedure yields fluorescent filaments with a biotinylated pointed end region. This filament solution was pipetted into a preassembled microfluidic chamber containing a neutravidin-conjugated coverslip (preparation described above), and equilibrated for 2-5 min before washing out free filaments with buffer using a syringe pump at a flow rate of 500 µL min^{-1} (2). A solution of 1 µM Mg^{2+}-actin monomers (15% were labeled with Alexa 488 or Alexa 647 and 20-40% were labeled with digoxigenin) was prepared in KMI buffer and immediately pipetted into the chamber, then incubated for 2 min before washing out with KMI. The final step was to pipette a mixture of anti-digoxigenin antibody-coated Dynabeads M-270 and 200 nM unlabeled Mg^{2+}-actin monomers in KMI buffer into the chamber.

The experimental design in the presence of cofilin was the same as with bare actin tethers up to the stage of Dyna beads conjugation. Prior to addition of Dyna beads, 2 µM of Alexa 488- *labeled S. cerevisiae* cofilin (saturating concentration; (5)) in KMI buffer was added to the chamber via a sample loop and incubated for 5-10 min with the flow turned off. Alexa 488-labeled cofilin was washed away with 2 µM of unlabeled cofilin in KMI containing 200 nM unlabeled actin monomers. Dynabeads M-270m beads coated with an anti-digoxigenin antibody suspended in the same solution as the previous wash buffer were subsequently added to the chamber via a sample loop.

Permanent Magnet Rotation
Four permanent magnets (Neodymium 0.5" × 0.5" × 0.5" SM Magnetics, C0501A) were rigidly mounted to a stepper motor (SparkFun Electronics, model number ROB-09238, controlled by stepper motor driver ROB-12779 and an Arduino Uno micro-controller) that was positioned in the microscope stage down-stream of the flow direction (as schematically illustrated in Figure 1A), 4.7 cm from the center of the microscope objective. The net pulling force exerted by the magnet on the paramagnetic beads, which scales with the magnetic field gradient, is very weak and negligible under our conditions, as assessed from effects on the random diffusion of free beads in solution (Figure S1). The holding force of the magnet, however, is strong and permits paramagnetic bead rotation with no detectable slipping between the bead and the motor rotation (Figure 1B-D; Movie S1-2).

Force Calibration
Since the paramagnetic beads used in force-extension and twist-extension are much larger in size with radius *r* = 1.4 µm (compared to actin filament girth of 10 nm), the pulling force (*f*) applied on a paramagnetic bead-conjugated actin filament by hydrodynamic flow is approximated to the pulling force

on the bead, which was determined from the flow rate-dependence of the fluid velocity (v) at beads center position and the distance (d) of the bead center from the flow chamber bottom (surface of coverslip) according to the Stokes-Einstein equation with Lorentz correction (Eq. S1) accounting for the effect of the surface of coverslip[*] (p314-315 of (6) and (7)):

Eq. S1
$$f(d,v) = -6\pi\eta r v\left(1 + \frac{9r}{16d}\right),$$

where η is the solution viscosity (1 cP), and r is the bead radius (1.4 µm). The minus sign indicates the pulling force (f) is in opposite direction to the fluid flow velocity (v). The fluid flow in the flow chamber is Poiseuille flow (8) and v is not a uniform constant, but depends on its distance (d) from the surface of coverslip as in Eq. S2 (p34 and p328 of (6), p52 of (9) and (8, 10, 11)):

Eq. S2
$$v(d) = 4V_m\frac{d}{h}\left(1 - \frac{d}{h}\right) = \frac{6Qd}{wh^2}\left(1 - \frac{d}{h}\right) \sim \frac{6Qd}{wh^2} \quad \text{when } d \ll h.$$

In Eq. S2, h is the height of the flow chamber used in our experiments (measured as 150.3 ($\pm$1.9) µm; discussed below), V_m is the maximum flow velocity at the center ($\frac{h}{2}$) of the chamber, Q is volumetric fluid flow rate, and w (~ 2 mm) is the flow chamber width. The relation $Q = 2whV_m/3$ (8, 10, 11) is used in the last equality. Eq. S2 indicates the value of v depends approximately linearly on d when $d \ll h$, and scales linearly with the flow rate (Q), which indicates the flow-mediated pulling force on the beads (f) also scales linearly with the flow rate (Q). Eq. S2 can also be used to obtain the flow chamber height h from the slope of the linear dependence of the measured v vs. R.

In our force- and twist-extension experiments, beads are on the surface of the coverslip and the distances of their centers away from the surface are given by the radius of the beads ($d = r$ =1.4 µm). In this case, the fluid velocity at the bead center position $v(r)$ is directly measured by the untethered bead velocity (v; Figure S1). The positions of untethered beads moving across the microfluidic channel over a range of hydrodynamic flow rates were tracked in ImageJ using the *TrackMate* plugin (12). Since beads are non-buoyant in water, they move along the chamber surface. In addition, the camera focus was adjusted to the surface. Hence, the beads too far from the bottom of the chamber would be out of focus and not be tracked. In short, the flow velocity measured by the untethered beads velocity is at the bead center height equal to the bead radius $d = r$. The bead velocity distributions at all flow rates were very well fitted to Gaussian distribution (Figure S1E and F are representations of velocity distributions under low and high flow rates), supporting our assumption that beads moved at a constant distance from the surface. If beads moved at varying distances from the surface, the bead velocity histogram should be asymmetric, biased toward the high velocity side as defined by Eq. S2. The pulling force on beads on the bottom of chamber $f(r)$ can be calculated directly with the measured flow velocity

---

[*]*Footnote*: Our rectangular flow chamber can be approximated to two parallel infinite walls. The non-slip boundary requirements at the walls make flow velocity between the walls non uniform and also interfere with streamline flow shape and therefore the pulling force from the flow exerted on the bead, which need be accounted for. Unfortunately, the pulling force by flow on a sphere under parallel walls has not been explicitly solved for general cases (§7-4 of (6)). Since in our experiments, beads are close to one wall and far away from the other (i.e., d/h ~0.01 $\ll$ 1), we can treat our case as a sphere near one infinite wall rather than between two walls or a sphere in a pipe whose diameter is comparably very large compared to the bead (i.e. infinite pipe diameter)).

Both approximations give the same correction factor of $\left(1 + \frac{9r}{16d}\right)$ (§7-3 of (6)) in Eq. S1.

according to Eq. S1 with $d = r$. The linear fit of f vs. Q serves as a force calibration curve in our study (Figure S1D).

In our twist-extension experiments, the rotating bead occasionally wobbled slightly, and the estimated bead center height from flow chamber bottom, by image blur due to out-of-focus, changes in the range of r to $< 2r = 2.8$ µm. According Eq. S1 and S2, the flow velocity and pulling force on bead at $d = 2r$ are $v(2r) \sim 2v(r)$ and $f(2r, 2v) = (2.56/1.56)f(r, v) \sim 1.64\,f(r, v) < 2\,f(r, v)$.

Model for Filament Twist-Extension

To describe the twist-extension behavior of actin filaments, an analytical two-state model developed for DNA (13) was modified for actin filaments. In the model, it is assumed that a filament subunit exists in one of two states when a filament is twisted: plectonemic or non-plectonemic (linear). We define twist density (σ) as the number of applied rotations per unit filament length (units of rot µm^{-1}). We note that in the DNA literature, the symbol σ is used to define the relative change in linking number, given by the change in linking number (ΔLk) divided by the intrinsic linking number (number of rotations in relaxed conformation, Lk_0).

The experimental data being used to extract the mechanical properties of actin filaments is R/L as a function of twisting and pulling. From thermodynamic principles (13, 14), the value of R/L is related to the filament free energy density (F, in units of $k_B T$ per unit length) and the applied pulling force (f) as follows:

Eq. S3
$$\frac{R}{L} = -\frac{\partial F}{\partial f}.$$

In the non-plectonemic state, the term F is the sum of contributions from pulling and twisting (13):

Eq. S4
$$F = -g + \frac{1}{2}L_{TS}\sigma^2.$$

In this form, g represents the free energy density associated with pulling, whereas the second term represents the energy density associated with twisting.

Under conditions where $L_B f \gg k_B T$ (13, 15), integration of Eq. 2 in the main text with respect to force yields the free energy density associated with pulling (g) as a function of the pulling force f:

Eq. S5
$$g \sim f - \sqrt{\frac{k_B T f}{L_B}} \mp \frac{k_B T \ln f}{2}\overline{\left(\frac{1}{L}\right)}.$$

The second term in Eq. S4 reflects contributions from twisting. The term L_{TS} in Eq. S4 is proportional to the effective torsional stiffness ($L_{T,eff}k_B T$) according to:

Eq. S6
$$L_{TS} = (L_{T,eff}k_B T)\omega_0^2.$$

Here, $\omega_0 = 2\pi$ is for unit conversion of σ so that $\sigma\omega_0$ is equal to the twist density in rad μm^{-1}. The effective torsional persistence length $L_{T,eff}$ depends on the "true" torsional persistence length L_T and the applied pulling force according to:

Eq. S7
$$L_{T,eff} = \frac{L_T}{1 + \frac{L_T}{4L_B}\sqrt{\frac{k_B T}{f L_B}}} \xrightarrow{f \to \infty} L_T.$$

The value of $L_{T,eff}$ is smaller than L_T (i.e., appears more compliant) because thermal bending dissipates the applied torsional strain. High pulling force (f) dampens thermal bending and $L_{T,eff}$ approaches L_T. The partial derivative of the free energy density in Eq. S4 with respect to force f yields the relative end-to-end distance of the filament prior to plectoneme formation according to:

Eq. S8
$$\frac{R}{L} = 1 - \frac{1}{2}\sqrt{\frac{k_B T}{L_B f}} + \frac{k_B T}{2f}\overline{\left(\frac{1}{L}\right)} - \frac{\omega_0^2 \sigma^2}{\left(\frac{4L_B}{L_T}\sqrt{\frac{f L_B}{k_B T}}+1\right)^2}\sqrt{\frac{k_B T L_B^3}{f}}, \quad |\sigma| < |\sigma_s|.$$

In the equation, σ_s is a special applied twist density at which filaments form plectonemes (referred to as critical twist density). The torque prior to plectoneme formation (τ) can be expressed as the following (13):

Eq. S9
$$\tau = (L_{Ts}/\omega_0)\sigma, \qquad |\sigma| < |\sigma_s|.$$

Twisted filaments plectoneme at the twist density σ_s (provided the pulling force is sufficiently low; Figure 3). A filament with a plectoneme consists of a mixture of plectonemic and non-plectonemic regions. The fraction of plectonemic regions increases linearly with twist density and does not contribute to R/L. Eq. S10 gives the force-dependence of R/L, contributed from only the fraction in the non-plectonemic state (13):

Eq. S10
$$\frac{R}{L} = \begin{cases} 1 - \frac{1}{2}\sqrt{\frac{k_B T}{L_B f}} + \frac{k_B T}{2f}\overline{\left(\frac{1}{L}\right)} - \frac{\omega_0^2 \sigma^2}{\left(\frac{4L_B}{L_T}\sqrt{\frac{f L_B}{k_B T}}+1\right)^2}\sqrt{\frac{k_B T L_B^3}{f}}, & |\sigma| < |\sigma_s| \\ \frac{|\sigma_p|-|\sigma|}{|\sigma_p|-|\sigma_s|}\left(1 - \frac{1}{2}\sqrt{\frac{k_B T}{L_B f}} + \frac{k_B T}{2f}\overline{\left(\frac{1}{L}\right)} - \frac{\omega_0^2 \sigma_s^2}{\left(\frac{4L_B}{L_T}\sqrt{\frac{f L_B}{k_B T}}+1\right)^2}\sqrt{\frac{k_B T L_B^3}{f}}\right), & |\sigma_s| \leq |\sigma| < |\sigma_p| \\ 0, & |\sigma_p| \leq |\sigma| \end{cases}.$$

where the fraction of subunits in the non-plectonemic conformation is given by $\frac{|\sigma_p|-|\sigma|}{|\sigma_p|-|\sigma_s|}$. The term σ_p is applied twist density where the entire filament is plectonemic.

Conjugating Anti-Digoxigenin Paramagnetic Beads to Digoxigenin Marker Beads
To coat fluorescent marker beads with digoxigenin, a solution of 2 mg mL^{-1} BSA and 0.2 mg mL^{-1} BSA-Digoxigenin (CM5210, Cell Mosaic) was prepared in 5 mL of 50 mM MES. A 2% marker bead suspension (100 µL, TransFluoSpheres Carboxylate-Modified Microspheres, 1 µm, T8880, ThermoFisher) was then added and the solution was equilibrated at room temperature for 15 min. EDAC (1-Ethyl-3-(3-

Dimethylaminopropyl) carbodiimide, Hydrochloride; E2247, ThermoFisher) (40 mg) was dissolved in the bead suspension, the pH adjusted to 6.5, and the sample was gently rocked at room temperature for 2 h. The crosslinking reaction was quenched with glycine at a final concentration of 100 mM. After 30 min the beads were washed three times with 5 mL of 1X KMI (no DTT or ATP) and beads pelleted with centrifugation at 4000 x *g*. The washed beads were suspended in 100 μL of 1X KMI. Marker beads were added 1:1 to a solution of anti-digoxigenin paramagnetic beads (see above) and equilibrated for 1 h with gentle pipetting every 5 min.

Modeling Thermally-Driven, Filament Twist Fluctuations

The rotational strain energy (E_{rot}) of a uniform, twisted biopolymer of length L can be written as:

Eq. S11
$$\frac{E_{rot}}{k_B T} = \int_0^L \frac{1}{2} L_T \left(\frac{d\emptyset}{ds}\right)^2 ds,$$

where s is the segment contour length and $\frac{d\emptyset}{ds}$ is the local, rotational angle change density by thermally driven fluctuations. Dividing the biopolymer to N equal-length segments ds, the total rotational energy can be expressed as:

Eq. S12
$$\frac{E_{rot}}{k_B T} = \frac{1}{2} L_T \sum_{i=1}^{N} \left(\frac{\Delta\emptyset_i}{\Delta s}\right)^2 \Delta s.$$

The partition function for a biopolymer in the Canonical distribution at the fixed temperature T is

Eq. S13
$$Z = \sum_{\{\Delta\emptyset_1, \Delta\emptyset_2, \dots, \Delta\emptyset_N\}} e^{-\frac{E}{k_B T}} = \sum_{\{\Delta\emptyset_1\}} \sum_{\{\Delta\emptyset_2\}} \dots \sum_{\{\Delta\emptyset_N\}} e^{-\frac{1}{2} L_T \sum_i \frac{\Delta\emptyset_i^2}{\Delta s}}$$
$$= \sum_{\{\Delta\emptyset_1\}} \sum_{\{\Delta\emptyset_2\}} \dots \sum_{\{\Delta\emptyset_N\}} \prod_i e^{-\frac{1}{2} L_T \frac{\Delta\emptyset_i^2}{\Delta s}}$$
$$= \sum_{\{\Delta\emptyset_1\}} e^{-\frac{1}{2} L_T \frac{\Delta\emptyset_1^2}{\Delta s}} \sum_{\{\Delta\emptyset_2\}} e^{-\frac{1}{2} L_T \frac{\Delta\emptyset_2^2}{\Delta s}} \dots \sum_{\{\Delta\theta_N\}} e^{-\frac{1}{2} L_T \frac{\Delta\emptyset_N^2}{\Delta s}} = z^N,$$

where the sum over $\Delta\Phi_i$ means over all possible angle changes between two adjacent segments from $-\pi$ to π. Since the segment length Δs << $L_T\pi^2$, and the value of $e^{-\frac{1}{2} L_T \frac{\pi^2}{\Delta s}} \sim 0$ at $\Delta\Phi = \pm\pi$, the $\Delta\Phi$ range can be extended from $\pm\pi$ to $\pm\infty$. The partition function for each small segment then becomes:

Eq. S14
$$z = \sum_{\{\Delta\emptyset_i\}} e^{-\frac{1}{2} L_T \frac{\Delta\emptyset_i^2}{\Delta s}} \rightarrow \int_{-\infty}^{\infty} e^{-\frac{1}{2} L_T \frac{\Delta\emptyset_i^2}{\Delta s}} d(\Delta\emptyset_i)$$
$$\left(let\ t = \frac{1}{2} L_T \frac{\Delta\emptyset_i^2}{\Delta s}, \Delta\emptyset_i = \sqrt{2t\frac{\Delta s}{L_T}}, d(\Delta\emptyset_i) = \frac{1}{2}\sqrt{2\frac{\Delta s}{L_T}} t^{-\frac{1}{2}} dt \right)$$
$$= 2\frac{1}{2}\sqrt{2\frac{\Delta s}{L_T}} \int_0^{\infty} t^{-\frac{1}{2}} e^{-t}\, dt$$
$$= \sqrt{2\pi\sigma^2}$$

where $\sigma^2 = \frac{\Delta s}{L_T}$. The probability density function of relative twist (P) at the i_{th} segment is now given by:

Eq. S15 $P\left(\Delta\emptyset, \frac{\Delta s}{L_T}\right) = P(\Delta\emptyset_i, \sigma) = \frac{1}{Z}e^{-\frac{1}{2}L_T\frac{\Delta\emptyset_i^2}{\Delta s}}\sum_{\{\Delta\emptyset_1\}}\sum_{\{\Delta\emptyset_2\}}\cdots\sum_{\{\Delta\emptyset_{i-1}\}}\sum_{\{\Delta\emptyset_{i+1}\}}\cdots\sum_{\{\Delta\emptyset_N\}}e^{-\frac{1}{2}L_T\sum_{j\neq i}\frac{\Delta\emptyset_j^2}{\Delta s}}$

$= e^{-\frac{1}{2}L_T\frac{\emptyset\theta_i^2}{\Delta s}}\dfrac{\sum_{\{\Delta\emptyset_1\}}\sum_{\{\Delta\emptyset_2\}}\cdots\sum_{\{\Delta\emptyset_{i-1}\}}\sum_{\{\Delta\emptyset_{i+1}\}}\cdots\sum_{\{\Delta\emptyset_N\}}e^{-\frac{1}{2}L_T\sum_{j\neq i}\frac{\Delta\emptyset_j^2}{\Delta s}}}{\sum_{\{\Delta\emptyset_1\}}\sum_{\{\Delta\emptyset_2\}}\cdots\sum_{\{\Delta\emptyset_N\}}e^{-\frac{1}{2}L_T\sum_{j}\frac{\Delta\emptyset_j^2}{\Delta s}}}$

$= \dfrac{e^{-\frac{1}{2}L_T\frac{\Delta\emptyset_i^2}{\Delta s}}}{\sum_{\{\Delta\emptyset_i\}}e^{-\frac{1}{2}L_T\frac{\Delta\emptyset_i^2}{\Delta s}}}$

$= \frac{1}{\sqrt{2\pi\sigma^2}}e^{-\frac{1}{2}\left(\frac{\Delta\emptyset_i}{\sigma}\right)^2}.$

This is a Gaussian distribution and the relative twist $\Delta\Phi$ between any adjacent subunits anywhere along the filament is a normally distributed random variable with an average twist angle change of 0 and a variance of σ^2. Please note, $\Delta\Phi_i$ is only the thermally driven relative twist and does not include the intrinsic twist between subunits. For the polymer with an intrinsic twist $\Delta\Phi_0$ between subunits (e.g., in cryo-EM analysis, structurally actin filament has an intrinsic twist ~ 166 deg sub^{-1} (16, 17)), the intrinsic twist needs to be subtracted from the observed twist before using Eq. S15. Alternatively, Eq. S15 can be modified to accommodate an intrinsic twist included in the observed twist as

Eq. S16 $$P\left(\Delta\emptyset_i, \frac{\Delta s}{L_T}\right) = \frac{1}{\sqrt{2\pi\sigma^2}}e^{-\frac{1}{2}\left(\frac{\Delta\emptyset_i - \Delta\emptyset_0}{\sigma}\right)^2}.$$

In this case, the Gaussian twist angle distribution has a mean value that is the intrinsic twist. The observed rotation angle (Φ_{obs}) about the filament axis of any subunit relative to a given reference frame is the sum of the true angle (Φ_i) plus a random detection noise (ε_i), such that the observed change in angle between two adjacent subunits is:

Eq. S17 $$\Delta\emptyset_{i,obs,2} = \emptyset_{i+1} + \varepsilon_{i+1} - \emptyset_i + \varepsilon_i = \Delta\emptyset_{i,2} + \varepsilon_{i+1} + \varepsilon_i,$$

$\Delta\Phi_{i,2}$ is the true relative twist between 2 subunits i and $i+1$. Similarly, the observed change in angle between 3 and 4 subunits is:

Eq. S18 $\Delta\emptyset_{i,obs,3} = (\emptyset_{i+2} + \varepsilon_{i+2}) - (\emptyset_i + \varepsilon_i)$
$= (\emptyset_{i+2} + \varepsilon_{i+2}) - (\emptyset_{i+1} + \varepsilon_{i+1}) + (\emptyset_{i+1} + \varepsilon_{i+1}) - (\emptyset_i + \varepsilon_i)$
$= \Delta\emptyset_{i+1,obs,2} + \Delta\emptyset_{i,obs,2}$
$= (\emptyset_{i+2} - \emptyset_{i+1} + \emptyset_{i+1} - \emptyset_i) + \varepsilon_{i+2} - \varepsilon_i$
$= \Delta\emptyset_{i+1,2} + \Delta\emptyset_{i,2} + \varepsilon_{i+2} - \varepsilon_i$

Eq. S19 $\Delta\emptyset_{i,obs,4} = (\emptyset_{i+3} + \varepsilon_{i+3}) - (\emptyset_i + \varepsilon_i)$
$= (\emptyset_{i+3} + \varepsilon_{i+3}) - (\emptyset_{i+2} + \varepsilon_{i+2}) + (\emptyset_{i+2} + \varepsilon_{i+2}) - (\emptyset_{i+1} + \varepsilon_{i+1}) +$
$(\emptyset_{i+1} + \varepsilon_{i+1}) - (\emptyset_i + \varepsilon_i)$

$$= \Delta\emptyset_{i+2,obs,2} + \Delta\emptyset_{i+1,obs,2} + \Delta\emptyset_{i,obs,2}$$
$$= (\emptyset_{i+3} - \emptyset_{i+2} + \emptyset_{i+2} - \emptyset_{i+1} + \emptyset_{i+1} - \emptyset_i) + \varepsilon_{i+3} - \varepsilon_i$$
$$= \Delta\emptyset_{i+2,2} + \Delta\emptyset_{i+1,2} + \Delta\emptyset_{i,2} + \varepsilon_{i+3} - \varepsilon_i.$$

Generalizing for the distance between any two subunits spaced n subunits apart yields:

Eq. S20 $\quad\quad \Delta\emptyset_{i,obs,n+1} = (\emptyset_{i+n} - \varepsilon_{i+n}) - (\emptyset_i + \varepsilon_i) = \sum_{j=1}^{n}\Delta\emptyset_{i+j-1,obs,2}$
$$= \sum_{j=1}^{n}\Delta\emptyset_{i+j-1,2} + \varepsilon,$$

where the difference of two random noises $\varepsilon = \varepsilon_{i+n} - \varepsilon_i$ is a random number itself of the same class and independent of subunit position i and spacing n. Therefore, experimentally, $\Delta\Phi_{l,obs,n+1}$ can be calculated by a sum of all n observed relative twist differences and theoretically, it is a sum of n normally distributed TRUE random relative angle changes between adjacent subunits plus a random noise term.

According to the properties of the normal distribution, the sum of two normally distributed random variables is also a normally distributed random variable and its expected value and variance are sums of the expected values and variances, respectively, of the two random variables (18). It can be shown that this property can be generalized to the sum of any number of normally distributed random variables. Based on this property of the normal distribution, assuming that the random number ε is also a normally distributed variable with variance σ_ε^2 and an expected value of 0, the variance for the true angle difference between two subunits spaced n subunits apart is $\sigma_{n+1}^2 = n\sigma^2 = (n\Delta s)/L_T$ where Δs is the spacing between adjacent subunits, i.e., the length of a subunit = 2.7 nm for actin (19), and the variance of the observed angle between n subunits is:

Eq. S21 $\quad\quad\quad\quad\quad\quad\quad\quad \sigma_{obs,n+1}^2 = n\frac{\Delta s}{L_T} + \sigma_\varepsilon^2.$

In whole filament twisting fluctuation experiments (Figure 4A) we measure the relative angle change between the two filament attachment points (at surface and at bead, length L), such that $n\Delta s = L$ and Eq. S21 takes the following form:

Eq. S22 $\quad\quad\quad\quad\quad\quad\quad\quad \sigma_\theta^2 = L/L_T + \sigma_\varepsilon^2.$

In this experiment, we tracked the centers of the paramagnetic (x_p,y_p) and marker beads (x_m,y_m) to determine the instantaneous rotation angle of the paramagnetic bead (θ_{inst}). The angle between the line connecting the centers of the two beads and the x-axis was determined as:

Eq. S23 $\quad\quad\quad\quad\quad\quad \theta_{inst}(t) = \arctan(\frac{y_m - y_p}{x_m - x_p}),$

The values of $\theta_{inst}(t)$ were adjusted to the quadrants they belong from 0-2π according to the signs of $x_m - x_p$ and $y_m - y_p$.

Since the time between two consecutive image frames (Δt) is small, we assume the absolute value of the change in angle between image frames is less than π ($-\pi < \delta\theta_{inst} < \pi$). Then, the angle at any time t

relative to time $t = 0$ is the cumulative sum of all the angle changes between previous frames and is given by:

Eq. S24
$$\theta(t) = \sum_{i=1}^{n} \delta\theta_{inst}(i\Delta t).$$

The mean subtracted absolute rotation angle then becomes (Figure 4D):

Eq. S25
$$\Delta\theta(t) = \theta(t) - <\theta(t)>.$$

Here, $<\theta(t)>$ is the average of all $\theta(t)$.

The torsional persistence length L_T is inversely proportional to the variance of the absolute angular fluctuations at equilibrium (Eq. S22). At times sufficiently long to sample the equilibrium distribution, indicated by plateau of the variance (Figure 4E), the variance of the angle calculated with Eq. S25 approaches Eq. S22 and the following applies ((20-22)):

Eq. S26
$$\sigma^2_{\theta(t\to\infty)} = <\Delta\theta(t\to\infty)^2> = L/L_T.$$

Here we neglect the detection noise (σ^2_ε) because it was > 100-fold smaller than the variance of the observed rotation angle ($\sigma^2_{\theta(t\to\infty)}$) for the filament lengths evaluated ($L\sim L_T$; $\sigma^2_\varepsilon < 0.0075$ vs. $\sigma^2_{\theta(t\to\infty)} \sim 1$). Eq. S26 shows that the variance of angular thermal rotation fluctuation of the whole polymer scales with polymer length linearly, which was pointed out by other groups as well (20, 21). The relation has been demonstrated for actin filaments by experimental observation (20, 21).

Modeling Actin Filament Fragmentation
The fragmentation of actin filaments during twist-extension experiments was modeled as a stochastic process with a loading rate (ωt, magnet rotation rate)-dependent rate-constant. In our experiments a stepper motor takes discrete steps as it twists an actin filament. Let the time between each motor step be Δt and the absolute angular position of the end of the filament is $\theta(t) = \omega t$. Because the magnet takes discrete steps, t is a discrete variable with spacing Δt, ($t = 0, \Delta t, 2\Delta t, 3\Delta t, ...$). The rotational strain energy for a given filament segment with length Δs ($E_{rot,seg}$) at any ωt is given by:

Eq. S27
$$\frac{E_{rot,seg}(\omega t)}{k_B T} = \frac{\Delta s\, L_T}{2L^2}(\omega t)^2.$$

Using the Arrhenius equation (23), the strain-dependent severing rate-constant ($k_{fragseg,strain}$) for this segment can be written as:

Eq. S28
$$k_{frag,seg,strain}(\omega t) = k_{frag,seg,native}\ \exp(E_{rot,seg}(\omega t)/k_B T),$$

where $k_{fragseg,native}$ is the intrinsic severing rate-constant per Δs. If choosing $\Delta s = 2.7$ nm as actin subunit length, a reported $k_{fragseg,native} = 5\times10^{-7}$ sub^{-1}s^{-1} (23). The probability that a given, strained segment will survive (i.e., not sever) over a Δt interval, $P_{nofrag,seg}(\omega t, \Delta t)$ is given by (23):

Eq. S29
$$P_{nofrag,seg}(\omega t, \Delta t) = \exp(-\Delta t k_{frag,seg,strain}(\omega t)).$$

The probability that none of the $n = L/\Delta s$ segments in the filament sever at time t over Δt time is the product of the survival probabilities of the whole filament:

Eq. S30
$$P_{nofrag_{fil}}(\omega t, \Delta t) = \prod_{i=1}^{n} \exp\left(-\Delta t k_{frag,seg,strain,i}(\omega t)\right)$$
$$= \exp(-\Delta t n k_{frag,seg,strain}(\omega t))$$
$$= \exp(-\Delta t \frac{L}{\Delta s} k_{frag,seg,strain}(\omega t)).$$

The probability that a filament will survive over the time of twist initiation ($t = 0$) and arbitrary time t is given by the product of all the survival probabilities at different time steps $t_i = i\Delta t$ between 0 and time t:

Eq. S31
$$P_{nofrag_{fil}}(\{\omega t_i\}, \Delta t) = \prod_{t_i=0}^{t} \exp\left(-\Delta t \frac{L}{\Delta s} k_{frag,seg,strain}(\omega t_i)\right)$$
$$= \exp\left(-\frac{L}{\Delta s} \sum_i \Delta t \, k_{frag,seg,strain}(\omega t_i)\right)$$
$$\xrightarrow{\Delta t \to 0} \exp\left(-\frac{L}{\Delta s} \int_0^t k_{frag,seg,strain}(\omega t) dt\right).$$

There is no analytical solution for the continuous, integrated form of Eq. S31, so the survival probabilities were calculated using numerical methods.
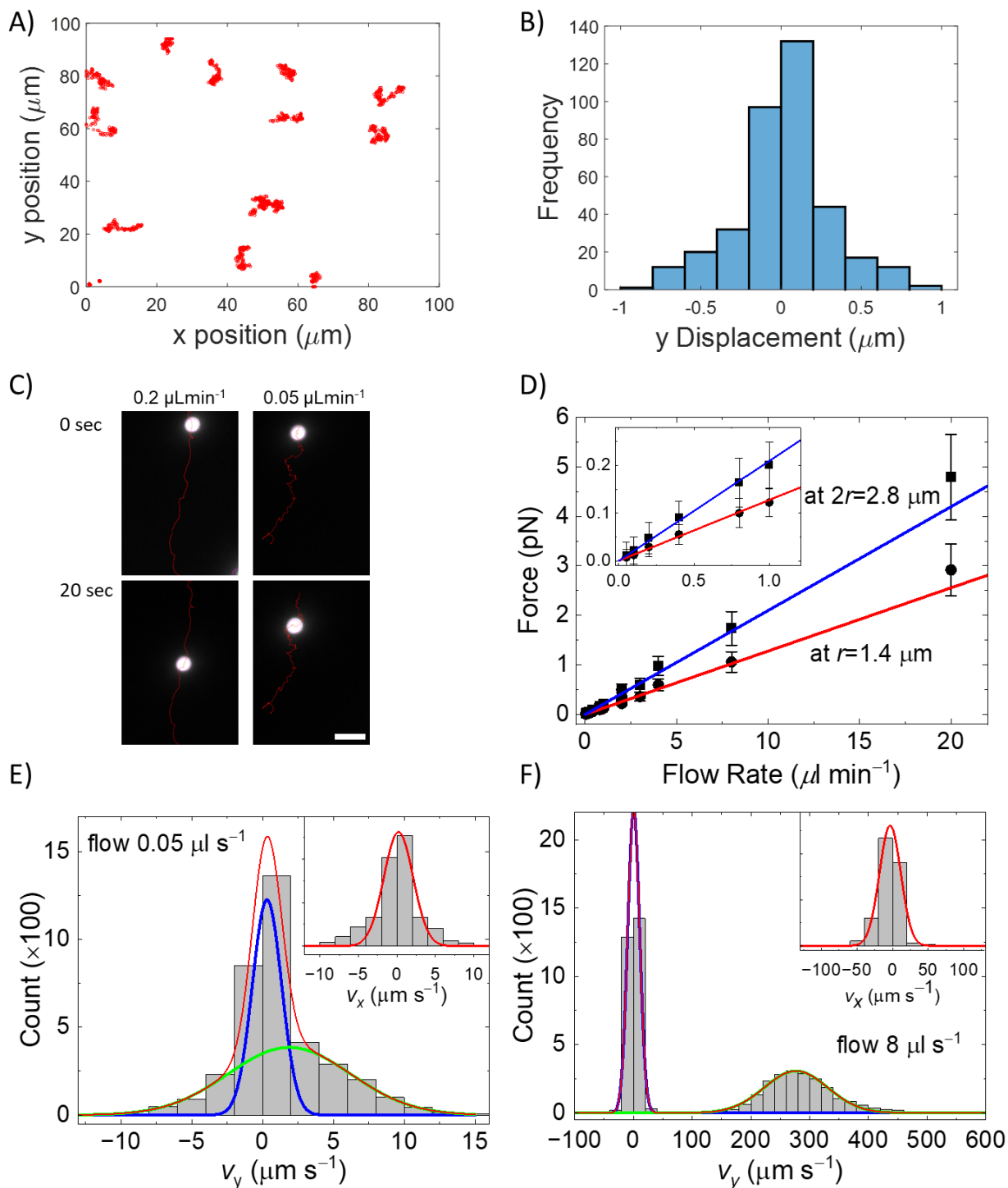
Supplemental Figure S1: A) Trajectories of paramagnetic beads under magnetic field randomly moving in solution in *xy* plane with no fluid flow, imaged every second. The magnetic field gradient is along the *y*-axis (magnet is positioned at the top of the field of view). B) Histogram of instantaneous bead displacements from (A) in the direction of the magnetic field gradient (*y*-direction) is centered at 0 and unbiased, indicating that the pulling force exerted by the magnet is negligible. C) Images of

paramagnetic beads moving across the surface of the microfluidic chamber at two time points 20 seconds apart under 0.2 (left) or 0.05 (right) µL min^{-1} flow rates. D) Force calibration curves, red and blue lines, used to relate the applied flow rate and the applied force on the beads at a height of their radius $z = r = 1.4$ µm (black dots) and at a height of 2 times of the radius $z = r = 2.8$ µm (black squares) away from the coverslip surface calculated using Eq. S1. Uncertainty bars are the standard deviation. Each applied flow rate corresponds to > 10 beads with a complete data set of 422 beads. E) and F) Distribution histograms of beads velocities between adjacent frames in the y and x axes (insets) under a flow rate of 0.05 (E) and 8 µL s^{-1} (F) for demonstration. The flow direction was along y axis. Therefore, the beads' movement in the y direction is flow-driven and the distribution was very well fitted by a double Gaussian peak function. The Gaussian peak centered at 0 represents immobile beads that were not moving (blue peak), whereas, the other Gaussian peak (green peak) represents the bead velocity distribution, in which the peak center is the average velocity in y-axis and the peak half width is the standard deviation. Bead movement in the x-axis is thermally-driven and random, and the distributions were well fitted by a Gaussian including both immobile and freely mobile beads (insets in E and F, histogram of velocity in x-axis).

OT 0.01 pN   UT 0.01 pN   OT 0.03 pN   UT 0.03 pN

Loop Radius (μm)
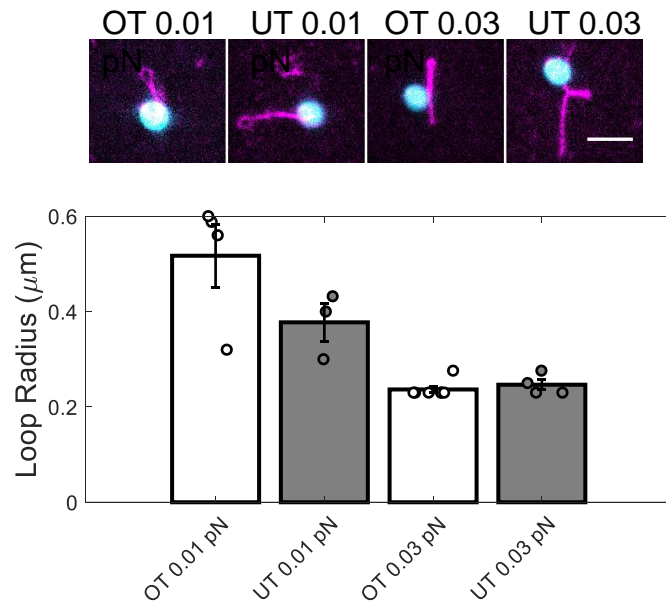
Supplemental Figure S2: Plectoneme end-loop size depends on the filament pulling force. Top panel: representative images of plectoneme loops at different pulling forces and twisting directions. Bottom panel: average loop radii for plectonemes at 0.01 and 0.03 pN of pulling force. Uncertainty bars represent standard errors of the mean.
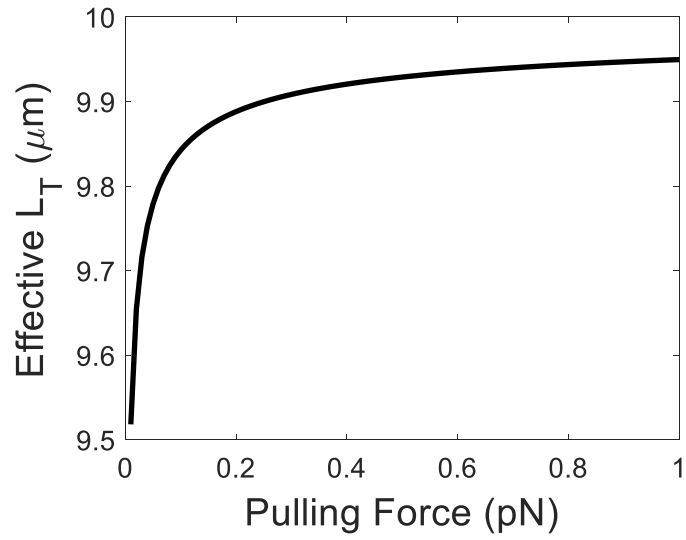
Supplemental Figure S3: The pulling force negligibly affects $L_{T,eff}$ of actin filaments over our force range. Model predicted relationship between $L_{T,eff}$ and the applied pulling force for actin filaments with L_B = 10 μm and L_T = 10 μm (Eq. S7).
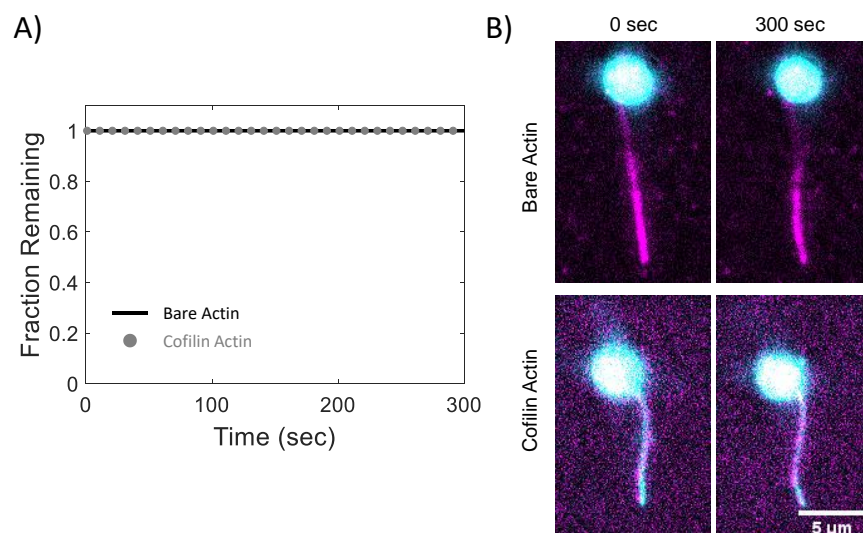
Supplemental Figure S4: Untwisted filaments do not sever over the time scales of our experiments. No fragmentation was observed for untwisted bare (black line) or untwisted, cofilin-saturated (gray circles) filaments over 5 minutes at flow rates of 0.2 µL min^{-1}, n=7 and 7, respectively. This is appreciably slower than fragmentation imposed by twisting which happens in less than a minute for both bare and cofilin-saturated filaments.
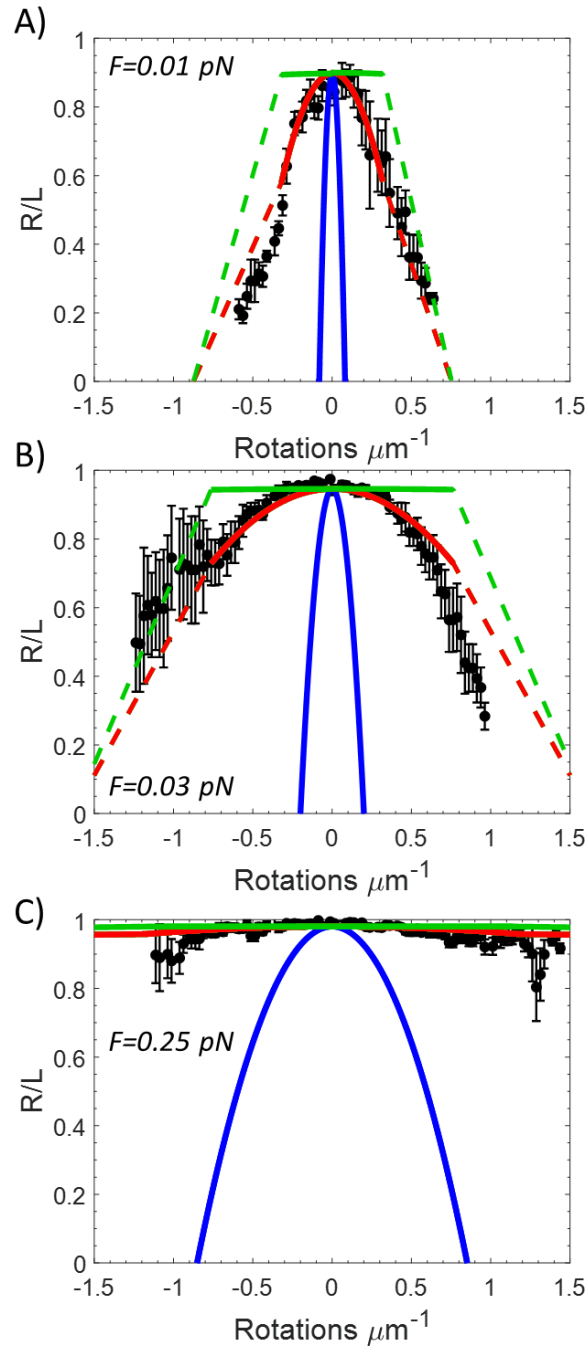
Supplemental Figure S5: Actin filament twist-extension curves simulated using Eq. 3 (main text) and S10 with different filament L_T values (green = 1 μm, red = 10 μm, and blue = 100 μm) and long axis pulling forces (A = 0.01 01 pN; B = 0.03 pN, and C = 0.25 pN) overlaying experimental data to illustrate the sensitivity of actin filament plectoneme-formation on the filament torsional stiffness. Filament lengths (L), σ_s, and σ_p were constrained to the experimentally observed values.
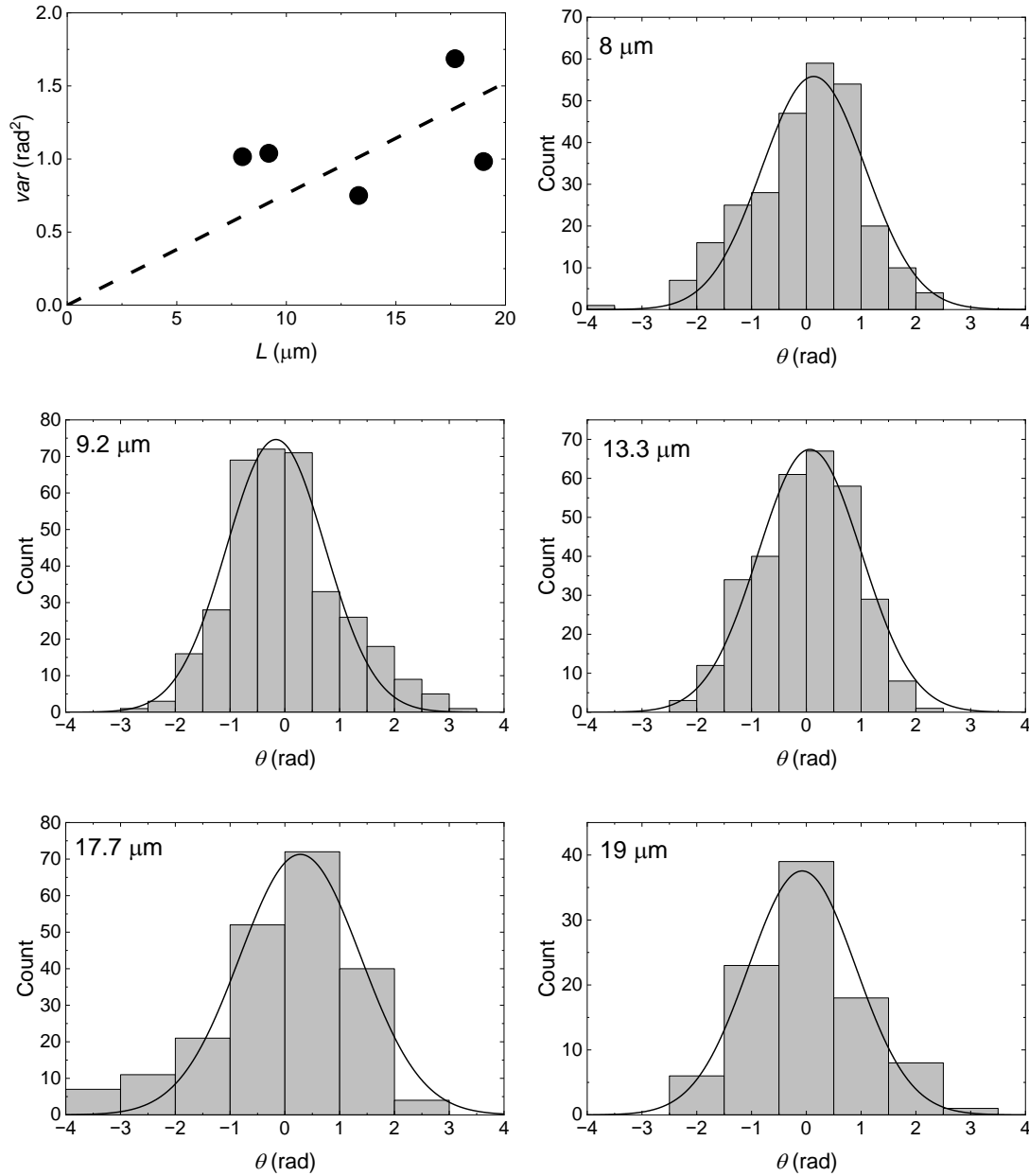
Supplemental Figure S6. Dependence of the observed twisting fluctuation variance on filament length. The experimental data in this plot are the same data as in Figure 4 of the main text. The distribution of observed filament rotation angles about the *z*-axis (Figure 4A), calculated by subtracting the mean angle such that the angles fluctuate about zero, show that the actin filament angles fluctuate around their means in Gaussian like manner (black solid lines represent best fits of the data to a Gaussian function). The dependence of the angular fluctuation variance on filament length (indicated in the individual panels) calculated from directly averaging (top left) shows how the observed variance varies with filament length. The dashed line through the data represents the length-dependence of the observed variance (Eq. 4) for a filament torsional stiffness of 13 μm.

Supplemental Movie Legends

Supplemental Movie 1: Phalloidin decorated actin filament attached to two paramagnetic beads is rotated (left). Cosine of the rotation angle of bead (black dots) and the magnet (red line) are in phase (right). Note that all movies are not played in real time.

Supplemental Movie 2: Alexa-647 actin filament (magenta) conjugated to a paramagnetic bead (cyan) rotates around the paramagnetic bead as the permanent magnet is rotated.

Supplemental Movie 3: Alexa-647 actin filament (magenta) conjugated to a paramagnetic bead (cyan) is subjected to a range of flow induced pulling forces, 0.007pN to 2.9pN.

Supplemental Movie 4: Alexa-647 actin filament (magenta) conjugated to a paramagnetic bead (cyan) is pulled with 0.03 pN of tension and twisted (left). Filament end-to-end distance is determined by tracking of the paramagnetic bead (right).

Supplemental Movie 5: Alexa-647 actin filament (magenta) conjugated to a paramagnetic bead (cyan) is pulled with 0.03 pN of tension and over-twisted until it supercoils. After supercoiling filament is under twisted until the filament twist is neutral.

Supplemental Movie 6: Alexa-647 actin filament (magenta) conjugated to a paramagnetic bead (cyan) is pulled with 0.03 pN of tension and does not fragment.

Supplemental Movie 7: Alexa-647 actin filament (magenta) conjugated to a paramagnetic bead (dim magenta) and a nonmagnetic marker bead (bright magenta). Flow is turned off, a cylindrical magnet is lowered into place, and the focal plane is adjusted to visualize the paramagnetic and marker beads.

Supplemental Movie 8: Alexa-647 actin filament (magenta) conjugated to a paramagnetic bead (cyan) is pulled with 0.25 pN of tension and over-twisted until it fragments.

Supplemental Movie 9: Alexa-647 actin filament (magenta) conjugated to a paramagnetic bead (cyan) is pulled with 0.03 pN of tension and over-twisted until it fragments.

Supplemental Movie 10: Alexa-647 actin filament (magenta) saturated with cofilin (cyan) is conjugated to a paramagnetic bead (cyan) and over-twisted until the filament fragments.

Supplemental Movie 11 Alexa-647 actin filament (magenta) saturated with cofilin (cyan) is conjugated to a paramagnetic bead (cyan) and under-twisted until the filament fragments.

Supplemental Movie 12: Rotational fluctuations of a surface tethered Alexa-647 actin filament conjugated to a paramagnetic bead (dim magenta) and a nonmagnetic marker bead (bright magenta). Filament is pulled straight perpendicular to the coverslip.

Supplemental References

1.   Y. Gidi, S. Bayram, C. J. Ablenas, A. S. Blum, G. Cosa, Efficient One-Step PEG-Silane Passivation of Glass Surfaces for Single-Molecule Fluorescence Studies. *ACS Appl Mater Interfaces* **10**, 39505-39511 (2018).
2.   N. G. Pandit *et al.*, Force and phosphate release from Arp2/3 complex promote dissociation of actin filament branches. *Proc Natl Acad Sci U S A* **117**, 13519-13528 (2020).
3.   E. M. Johnson-Chavarria, U. Agrawal, M. Tanyeri, T. E. Kuhlman, C. M. Schroeder, Automated single cell microbioreactor for monitoring intracellular dynamics and cell growth in free solution. *Lab Chip* **14**, 2688-2697 (2014).
4.   E. M. De La Cruz, Cofilin binding to muscle and non-muscle actin filaments: isoform-dependent cooperative interactions. *J Mol Biol* **346**, 557-564 (2005).
5.   B. R. McCullough *et al.*, Cofilin-Linked Changes in Actin Filament Flexibility Promote Severing. *Biophys J* **101**, 151-159 (2011).
6.   J. Happel, H. Brenner, *Low Reynolds number hydrodynamics: with special applications to particulate media*, Mechanics of fluids and transport processes (Martinus Nijhoff Publishers,, ed. 1st pbk., 1983), pp. 553 p.
7.   S. B. Smith, L. Finzi, C. Bustamante, Direct mechanical measurements of the elasticity of single DNA molecules by using magnetic beads. *Science* **258**, 1122-1126 (1992).
8.   A. Jegou, M. F. Carlier, G. Romet-Lemonne, Formin mDia1 senses and generates mechanical forces on actin filaments. *Nat Commun* **4**, 1883 (2013).
9.   L. D. Landau, E. M. Lifshits, *Fluid mechanics*, Course of theoretical physics (Pergamon Press, Oxford, England ; New York, ed. 2nd, 1987), pp. 539 p.
10.   N. Courtemanche, J. Y. Lee, T. D. Pollard, E. C. Greene, Tension modulates actin filament polymerization mediated by formin and profilin. *Proc Natl Acad Sci U S A* **110**, 9752-9757 (2013).
11.   J. Gorman, A. J. Plys, M. L. Visnapuu, E. Alani, E. C. Greene, Visualizing one-dimensional diffusion of eukaryotic DNA repair factors along a chromatin lattice. *Nat Struct Mol Biol* **17**, 932-938 (2010).
12.   J. Y. Tinevez *et al.*, TrackMate: An open and extensible platform for single-particle tracking. *Methods* **115**, 80-90 (2017).
13.   J. F. Marko, Torque and dynamics of linking number relaxation in stretched supercoiled DNA. *Phys Rev E* **76** (2007).
14.   L. D. Landau, E. M. Lifshitz, *Theory of elasticity* (Pergamon Press, Oxford New York, 1986), vol. 7.
15.   R. Phillips, *Physical biology of the cell* (Garland Science, London New York, NY, ed. Second edition /, 2013), pp. xxx, 1057 pages.
16.   A. R. Huehn *et al.*, Structures of cofilin-induced structural changes reveal local and asymmetric perturbations of actin filaments. *Proc Natl Acad Sci U S A* **117**, 1478-1484 (2020).
17.   A. Huehn *et al.*, The actin filament twist changes abruptly at boundaries between bare and cofilin-decorated segments. *J Biol Chem* **293**, 5377-5383 (2018).
18.   E. Kreyszig, *Advanced engineering mathematics* (John Wiley, Hoboken, NJ, ed. 9th, 2006).
19.   E. M. De La Cruz, M. L. Gardel, Actin Mechanics and Fragmentation. *J Biol Chem* **290**, 17137-17144 (2015).
20.   R. Yasuda, H. Miyata, K. Kinosita, Jr., Direct measurement of the torsional rigidity of single actin filaments. *J Mol Biol* **263**, 227-236 (1996).
21.   Y. Tsuda, H. Yasutake, A. Ishijima, T. Yanagida, Torsional rigidity of single actin filaments and actin-actin bond breaking force under torsion measured directly by in vitro micromanipulation. *Proc Natl Acad Sci U S A* **93**, 12937-12942 (1996).

22.   A. J. Hunt, J. Howard, Kinesin Swivels to Permit Microtubule Movement in Any Direction. *Proc Natl Acad Sci U S A* **90**, 11653-11657 (1993).
23.   A. C. Schramm, G. M. Hocky, G. A. Voth, J. L. Martiel, E. M. De La Cruz, Plastic Deformation and Fragmentation of Strained Actin Filaments. *Biophys J* 10.1016/j.bpj.2019.06.018, 453-463 (2019).